Computational Mechanics (2023) 71:853–866
https://doi.org/10.1007/s00466-022-02263-x

ORIGINAL PAPER

A fully implicit and thermodynamically consistent finite element framework for bone remodeling simulations

Maximilian Bittens[1] · **Udo Nackenhorst**[1]

Received: 1 July 2021 / Accepted: 10 December 2022 / Published online: 13 February 2023

Abstract
This work addresses the thermodynamically consistent formulation of bone remodeling as a fully implicit finite element material model. To this end, bone remodeling is described in the framework of thermodynamics for open systems resulting in a thermodynamically consistent constitutive law. In close analogy to elastoplastic material modeling, the constitutive equations are implicitly integrated in time and incorporated into a finite element weak form. A consistent linearization scheme is provided for the subsequent incremental non-linear boundary value problem, resulting in a computationally efficient description of bone remodeling. The presented model is suitable for implementation in any standard finite element framework with quadratic or higher-order element types. Two numerical examples in three dimensions are shown as proof of the efficiency of the proposed method.

Keywords Bone remodeling · Finite elements · Biomechanics · Thermodynamics with internal state variables

1 Introduction

Bone adapts to the loads under which it is placed. This phrase was stated in 1892 by Julius Wolff and is today referred to as *Wolff's law* [41]. In the following, many more researchers contributed to the theory and experimental validation of bone remodeling, among them [16,34], for examples. Based on these insights, connecting mechanical influences and biochemical reactions, many improvements in orthopedic treatment could be introduced into clinical practice.

Cowin and Hegedus [11] should be stated here as the first work to provide a closed mathematical description of bone remodeling. This was the starting point for bone remodeling simulations using finite elements, which has continued to be an active field of research in computational biomechanics throughout the last four decades. Despite promising results of even very early models [2,9,40], numerical instabilities, like the occurrence of *checkerboard-patterns*, were a recurring problem. Without stabilisation, those formulations were strongly mesh-dependent; refinement results in finer structures with subsequently smaller areas either adopting a prescribed minimum or maximum value for the bone mineral density. Many different approaches have been tried to achieve stability. In [22], for example, a node-based method was introduced, which successfully suppressed the checkerboard modes for linear elements with the density held constant per volume by averaging, which is related to the *superconvergent patch recovery* method [44]. Finally, Harrigan and Hamilton [19] showed under which conditions bone remodeling with E-ϱ-relations (cf. [10]) of the form

$$\frac{E}{E_0} = \left(\frac{\varrho}{\varrho_0}\right)^n, \quad E_0, \varrho_0, n \in \mathbb{R}, \tag{1}$$

have a stable and unique solution. By this time, three principle approaches for the remodeling stimulus were available in the literature: (1) the stress approach, (2) the fatigue damage approach, and (3) the strain energy density approach. Generalizing these ideas, [8] (cf. [38]) defined a daily remodeling stimulus

$$\Psi_\mathrm{d} = K \left[\sum_{i=1}^{N} n_i \Psi_i^m\right], \quad K, m \in \mathbb{R}, \tag{2}$$

✉ Maximilian Bittens
maximilian.bittens@ibnm.uni-hannover.de

[1] Institut für Baumechanik und Numerische Mechanik, Leibniz Universität Hannover, Appelstraße 9A, 30167 Hannover, Germany

with N different daily loading cases i, each with n_i repetitions and associated stimulus Ψ_i, and constants K and m. Choosing an appropriate stimulus Ψ_i the approaches (1), (2), and (3) can be recovered. Furthermore, it was shown that if Ψ is uniform in the bone, the three approaches lead to the same basic result. For more information, the reader is referred to the excellent review article [38].

From the more recent past, two different approaches should be mentioned here as examples: [24] and [17]. The former models bone adaption with a strain energy density stimulus built upon a profound theory for thermodynamically open systems, cf. [14,25], and the latter describes bone remodeling in analogy to damage mechanics. It is remarkable that even in the most recent contributions, the most prominent approach for time integration of the constitutive equations is the so-called "staggered"-approach (cf. [21,26,31,35,37]). This approach can be roughly defined by the following three steps: (1) solve a purely linear finite element model of the bone to obtain the mechanical stimulus at the nodes, (2) update the bone mineral densities at each node according to the discretized constitutive function and (3) update Young's modulus of each integration point according to the E-ϱ-relation. This procedure is repeated until convergence is achieved. The advantage of this approach is that no modifications of any finite element routines are necessary. The major disadvantage is the poor computational efficiency since explicit time-integration of the constitutive equations has to be performed.

It should be noted that there exists a variety of different approaches to achieve stability in computational bone remodeling, for example, [7,15], or [13]. However, all of the latter require some smoothing, averaging, or projection, making them difficult or impossible to implement as a standard finite element material model at the integration point level.

In this contribution, the integration point approach presented in [24] is adopted, but all steps are derived in close analogy to [12], which results in a thermodynamically consistent description of bone remodeling as an infinitesimal strain finite element material model with superior computational efficiency due to the fully implicit formulation. As a novel result, the inner local Newton iteration present in the integration point-based approach in [24] can be omitted.

2 Constitutive theory

The following briefly summarizes some essential relations between thermodynamically open systems and constitutive modeling. For a complete review of the theory of thermodynamically open systems, the reader is referred to [25] or [23]. In addition, it should be noted here that there exist a set of fundamental principles of material theory, which has to be fulfilled by any constitutive model, for example, the principle of determinism or the principle of objectivity. The reader is referred to [12] or [33] for a complete description of constitutive modeling.

2.1 Balance of mass

The local version of the balance of mass for open systems can be stated

$$\mathrm{D}_t \varrho = \mathfrak{R} \tag{3}$$

as the equality of the rate of chance of the spatial mass density ϱ and a mass source $\mathfrak{R}$, which is left to be defined in Sect. 4. Many other bone tissue models with a balance of mass of type (3) can be found in the literature by, amongst others, [3,19,40]. The incorporation of a mass flux into the latter equation, as shown in [25], is omitted here. In doing so, the resulting set of governing equations would require a numerical discretization scheme, the solution of which would be much more costly. To the authors, this additional expenditure does not seem to be justified since for bone remodeling, both approaches lead to the same basic results, as shown in [24].

2.2 Dissipation inequality

Respecting the non-constant mass in an open system results in an additional *entropy source* $\mathcal{S}$, as shown in [29,36], or [14], for example. Against this background, [25] provided a free-energy density-based version of the *Clausius–Duhem* inequality for open systems of the form

$$\begin{aligned}&\boldsymbol{\sigma} : \mathrm{D}_t \boldsymbol{\varepsilon} - \varrho \mathrm{D}_t \psi - \varrho (S + \mathrm{D}_\theta \psi) \mathrm{D}_t \theta - \mathcal{S}\theta \\ &- \boldsymbol{Q} \cdot \nabla_{\boldsymbol{X}} \ln \theta \geq 0 \,,\end{aligned} \tag{4}$$

where $\boldsymbol{\varepsilon}$ is the linearized strain tensor, ϱ the mass density, ψ the specific *Helmholtz free energy* function, S the entropy, θ the absolute temperature, and $\boldsymbol{Q}$ the heat flux. The Clausius–Duhem inequality can be decomposed into a local term d^{loc}, typically referred to as *Clausius–Planck inequality*, and a conductive term d^{cond}, typically referred to as *Fourier inequality*. Both terms are required to hold separately:

$$\begin{cases} d^{\mathrm{loc}} = \boldsymbol{\sigma} : \mathrm{D}_t \boldsymbol{\varepsilon} - \varrho \mathrm{D}_t \psi - \varrho (S + \mathrm{D}_\theta \psi) \mathrm{D}_t \theta - \mathcal{S}\theta & \geq 0 \\ d^{\mathrm{con}} = -\boldsymbol{Q} \cdot \nabla_{\boldsymbol{X}} \ln \theta & \geq 0 \end{cases} . \tag{5}$$

Here, the assumption is made that all processes are modeled as isothermal processes. Due to that assumption the Clausius–Duhem inequality reduces itself to the local part d^{loc}, since $d^{\mathrm{con}} \geq 0$ holds if $\nabla_{\boldsymbol{X}} \ln \theta = \boldsymbol{0}$.

2.3 A thermodynamical consistent constitutive law for bone remodeling

Following [12], it will be assumed that the set of *state variables*

$$\{\varrho, \boldsymbol{\varepsilon}\} \tag{6}$$

determines the *thermodynamical state* for any time t at a point $\boldsymbol{X} \in \mathcal{B}_0$, where $\boldsymbol{\varepsilon}$ is the linearized strain tensor and ϱ is reinterpreted as the bone mass density. Consequently, the specific Helmholtz free energy $\psi = \psi(\varrho, \boldsymbol{\varepsilon})$ is dependent on the state variables. Using the relation (3), the material time derivative of the free-energy follows as

$$\begin{aligned} \mathrm{D}_t \psi(\varrho, \boldsymbol{\varepsilon}) &= \partial_\varrho \psi \, \mathrm{D}_t \varrho + \partial_{\boldsymbol{\varepsilon}} \psi : \mathrm{D}_t \boldsymbol{\varepsilon} \\ &= \partial_\varrho \psi \, \mathfrak{R} + \partial_{\boldsymbol{\varepsilon}} \psi : \mathrm{D}_t \boldsymbol{\varepsilon} \, . \end{aligned} \tag{7}$$

Inserting the above into the Clausius–Planck inequality $(5)_1$ yields

$$\begin{aligned} d^{\mathrm{loc}} = (\sigma - \varrho \, \partial_{\boldsymbol{\varepsilon}} \psi) : \mathrm{D}_t \, \boldsymbol{\varepsilon} - \varrho \, \partial_\varrho \psi \, \mathfrak{R} \\ - \varrho (S + \mathrm{D}_\theta \psi) \mathrm{D}_t \theta - \mathcal{S} \theta \geq 0 \, , \end{aligned} \tag{8}$$

from which the constitutive equations

$$\begin{aligned} &\boldsymbol{\sigma} = \varrho \, \partial_{\boldsymbol{\varepsilon}} \, \psi \, , \quad S = -\mathrm{D}_\theta \, \psi \, = 0, \quad \text{and} \\ &\mathcal{S} = -\varrho \frac{1}{\theta} \, \partial_\varrho \psi \, \mathfrak{R} \end{aligned} \tag{9}$$

are implied. By that procedure the fulfillment of the Clausius–Duhem inequality is guaranteed a priori. Concluding the above, the thermodynamically consistent constitutive law for isothermal bone remodeling can be stated as

$$\begin{cases} \psi = \psi(\varrho, \boldsymbol{\varepsilon}) \\ \sigma = \varrho \partial_{\boldsymbol{\varepsilon}} \, \psi \\ \mathrm{D}_t \, \varrho = \mathfrak{R} \\ \mathcal{S} = -\varrho \frac{1}{\theta} \, \partial_\varrho \psi \mathfrak{R} \end{cases} . \tag{10}$$

Since the constitutive model described above is only dependent on the history of the linearized strain and bone mineral density, it is possible to define the *constitutive initial value problem*: presuming the history of linearized strain $\boldsymbol{\varepsilon}(t)$, $t \in [t_0, T]$, and the initial value of the bone mineral density $\varrho(t_0)$ are known, find the history of $\boldsymbol{\sigma}(t)$ and $\varrho(t)$ such that the constitutive equations

$$\begin{cases} \boldsymbol{\sigma}(t) = \varrho(t) \, \partial_{\boldsymbol{\varepsilon}} \, \psi(\varrho(t), \boldsymbol{\varepsilon}(t)) \\ \mathrm{D}_t \, \varrho(t) = \mathfrak{R}(\varrho(t), \boldsymbol{\varepsilon}(t)) \end{cases} \tag{11}$$

hold for every $t \in [t_{(0)}, T]$ (c.f. [12]).

2.4 Density-weighted generalized Hooke's law

For isothermal processes the strain energy density function

$$\Psi(\varrho, \boldsymbol{\varepsilon}) = \varrho \, \psi(\varrho, \boldsymbol{\varepsilon}) \tag{12}$$

is defined by the product of the bone mineral density ϱ and the specific Helmholtz free energy ψ (see e.g. [42]). In bone remodeling, a quite common choice for the specific Helmholtz free energy

$$\psi = \left[\frac{\varrho}{\varrho_0}\right]^n \psi^{\mathrm{LE}} = \left[\frac{\varrho}{\varrho_0}\right]^n \frac{1}{\varrho} \left[\frac{\lambda}{2} (\mathrm{tr}(\boldsymbol{\varepsilon}))^2 + \mu \mathrm{tr}(\boldsymbol{\varepsilon}^2)\right] , \tag{13}$$

is based on a classical linear-elastic-type free energy function ψ^{LE} weighted by a relative density $(\varrho/\varrho_0)^n$, where the exponent n is typically varied between $1 \leq n \leq 3.5$, and λ and μ being Lamé constants, as shown in [10,18] or [25], for examples. This provides a redefinition of the Cauchy stress tensor as the density-weighted Cauchy stress tensor

$$\begin{aligned} \boldsymbol{\sigma} = \partial_{\boldsymbol{\varepsilon}} \Psi = \varrho \, \partial_{\boldsymbol{\varepsilon}} \psi = \left[\frac{\varrho}{\varrho_0}\right]^n \boldsymbol{\sigma}^{\mathrm{LE}} \\ = \left[\frac{\varrho}{\varrho_0}\right]^n (\lambda \mathrm{tr}(\boldsymbol{\varepsilon}) \mathbf{I} + 2\mu \boldsymbol{\varepsilon}) \, . \end{aligned} \tag{14}$$

The density-weighted material tensor can then be derived as

$$\mathbb{C} = \partial_{\boldsymbol{\varepsilon}} \boldsymbol{\sigma} = \left[\frac{\varrho}{\varrho_0}\right]^n \mathbb{C}^{\mathrm{LE}} = \left[\frac{\varrho}{\varrho_0}\right]^n (\lambda \mathbf{I} \otimes \mathbf{I} + 2\mu \mathbb{I}) \, . \tag{15}$$

Finally, analogous to the generalized Hooke's law for continuous media, its density-weighted counterpart can be stated as

$$\boldsymbol{\sigma}(\varrho) = \mathbb{C}(\varrho) : \boldsymbol{\varepsilon} \, . \tag{16}$$

2.5 Relation of bone density to mechanical properties

In numerous works, a relation between the bone mineral density and Young's modulus of bone, with the general form of equation (1), has been established (see, e.g. [10,18,30,32]). Here, E_0, ϱ_0, and n are left to be identified by experimental investigations and physical reasoning, an ongoing issue in the scientific community. In [27] following basic material properties for the E-ϱ-relation have been proposed:

$$\begin{aligned} &E_0 = 6500 \, \frac{N}{mm^2} \, , \quad \varrho_0 = 1 \, \frac{g}{cm^3} \, , \quad n = 2 \, , \quad \text{and} \\ &\varrho \in [0, 2] \, \left[\frac{g}{cm^3}\right] . \end{aligned} \tag{17}$$

It has been shown that this model fits experimental observations sufficiently and is therefore used here.

3 Finite element modeling

This section provides a finite element modeling approach for bone remodeling. Herein, great care was taken on the linearization of the weak form and the constitutive relations and their incorporation into a Newton-Raphson scheme.

3.1 Weak form

A strong form of the governing equations describing bone remodeling in the frame of small deformations and with respect to an *initial configuration* of a continuum body $\mathcal{B}_0$ can be stated as

$$\begin{cases} \mathrm{Div}(\boldsymbol{\sigma}) = \mathbf{0}\,, \\ \boldsymbol{\varepsilon} = \frac{1}{2}\left(\mathrm{Grad}(\boldsymbol{u}) + \mathrm{Grad}(\boldsymbol{u})^{\mathrm{T}}\right)\,, \\ \boldsymbol{\sigma} = \mathbb{C}(\varrho) : \boldsymbol{\varepsilon}\,. \end{cases} \tag{18}$$

Furthermore, the existence and uniqueness of a solution (cf. [39]) to the *strong form* (18) is only guaranteed with a suitable set of *boundary conditions* prescribed on $\partial\mathcal{B}_0$, namely *Dirichlet* boundary conditions on $\Gamma_u \subseteq \partial\mathcal{B}_0$ and *Neumann* boundary conditions on $\Gamma_\sigma = \partial\mathcal{B}_0 \backslash \Gamma_u$:

$$\begin{aligned} &\boldsymbol{u}(\boldsymbol{X},t) = \bar{\boldsymbol{u}}(\boldsymbol{X}) \quad \forall\, \boldsymbol{X} \in \Gamma_u \quad \text{and} \\ &\boldsymbol{t}(\boldsymbol{X},t) = \bar{\boldsymbol{t}}(\boldsymbol{X}) \quad \forall\, \boldsymbol{X} \in \Gamma_\sigma\,. \end{aligned} \tag{19}$$

Equation (19) is equivalent to demanding $\boldsymbol{u}$ to be a *kinematically admissible displacement field* and $\boldsymbol{\sigma}$ to be a *statically admissible stress field* (cf. [39]).

Applying the *principle of virtual work* and some mathematical manipulations results in a standard weak form for small strain elasticity

$$\delta\Pi = \delta U - \delta W = \int_{\mathcal{B}_0} \delta\boldsymbol{\varepsilon} : \boldsymbol{\sigma}\,\mathrm{d}V - \int_{\Gamma_\sigma} \delta\boldsymbol{u}\cdot\boldsymbol{t}\,\mathrm{d}A = 0\,. \tag{20}$$

3.2 Material non-linearities

Presuming a constant material tensor $\mathbb{C}$, the weak form (20) is a *linear boundary value problem* that in a finite element framework ultimately results in a linear system of algebraic equations. Obviously, the latter does not hold here since in bone remodeling $\mathbb{C} = \mathbb{C}(\varrho)$ is a density-weighted material tensor (see Sect. 2.4). The evolution of bone mineral density is described by the constitutive initial value problem given in equation (11), a constraint that has to be fulfilled in addition to the weak form. Therefore, the problem becomes a *nonlinear initial boundary value problem*:

$$\begin{cases} \delta\Pi(\varrho(t), \boldsymbol{u}(t)) = 0 \\ \Phi(\varrho(t), \boldsymbol{u}(t)) = \mathrm{D}_t\,\varrho(t) - \mathfrak{R}(\varrho(t), \boldsymbol{\varepsilon}(t)) = 0 \end{cases}, \tag{21}$$

with the prescribed *history* of Dirichlet boundary conditions

$$\boldsymbol{u}(\boldsymbol{X},t) = \bar{\boldsymbol{u}}(\boldsymbol{X},t) \quad \forall \boldsymbol{X} \in \Gamma_u\,,\ \forall t \in [t_0, T]\,, \tag{22}$$

the prescribed *history* of Neumann boundary conditions

$$\boldsymbol{t}(\boldsymbol{X},t) = \bar{\boldsymbol{t}}(\boldsymbol{X},t) \quad \forall \boldsymbol{X} \in \Gamma_\sigma\,,\ \forall t \in [t_0, T]\,, \tag{23}$$

and the *initial* internal bone mineral density field

$$\varrho(\boldsymbol{X}, t_0) = \varrho_0(\boldsymbol{X}) \quad \forall \boldsymbol{X} \in \mathcal{B}_0\,. \tag{24}$$

In general, the constitutive model is path-dependent, and for problem (21), a closed-form solution is not available. Choosing a backward Euler numerical integration scheme for the constitutive initial value problem (11) results in the definition of an *incremental* constitutive function for the bone mineral density

$$\varrho_{(n+1)} = \varrho_{(n)} + \Delta\varrho = \varrho_{(n)} + \Delta t\hat{\mathfrak{R}}(\varrho_{(n)}, \boldsymbol{\varepsilon}_{(n+1)})\,, \tag{25}$$

where $\hat{\mathfrak{R}}$ is the *algorithmic counterpart* of the mass source $\mathfrak{R}$ and $\Delta t = t_{(n+1)} - t_{(n)}$, and an *incremental* constitutive function for the stress tensor

$$\boldsymbol{\sigma}_{(n+1)} = \hat{\boldsymbol{\sigma}}(\varrho_{(n)}, \boldsymbol{\varepsilon}_{(n+1)}) = \mathbb{C}(\varrho_{(n)} + \Delta\varrho) : \boldsymbol{\varepsilon}_{(n+1)}\,. \tag{26}$$

As a next step, the above is reintroduced into the weak form (20), resulting in an *incremental* boundary value problem. Because within one time-step, the bone mineral density is held constant, we can think of $\delta\Pi_{(n+1)} = \delta\Pi(\boldsymbol{u}_{(n+1)})$ as a function of the unknown displacements $\boldsymbol{u}_{(n+1)}$ alone, which makes the constitutive model *path-independent* within one time-step:

$$\begin{aligned} \delta\Pi_{(n+1)} &= \delta U_{(n+1)} - \delta W_{(n+1)} \\ &= \int_{\mathcal{B}_0} \delta\boldsymbol{\varepsilon} : \mathbb{C}(\varrho_{(n)} + \Delta\varrho) : \boldsymbol{\varepsilon}_{(n+1)}\,\mathrm{d}V \\ &\quad - \int_{\Gamma_\sigma} \delta\boldsymbol{u}\cdot\boldsymbol{t}_{(n+1)}\,\mathrm{d}A = 0\,. \end{aligned} \tag{27}$$

The above is a non-linear equation and needs consistent linearization in order to be solved via a *Newton-Raphson* scheme.

3.3 Linearization

Presuming the displacement field $\boldsymbol{u}_{(n)}$ is known and $\delta\Pi$ is sufficiently smooth in t, a expression for the unknown virtual work

$$\delta\Pi_{(n+1)} = \delta\Pi(\boldsymbol{u}_{(n+1)}) = \delta\Pi(\boldsymbol{u}_{(n)} + \Delta\boldsymbol{u})\,, \tag{28}$$

can be derived at time-step $t_{(n+1)} = t_{(n)} + \Delta t$ and $\boldsymbol{u}_{(n+1)} = \boldsymbol{u}_{(n)} + \Delta\boldsymbol{u}$ by truncating a *Taylor series expansion*:

$$\begin{aligned}\delta\Pi(\boldsymbol{u}_{(n)} + \Delta\boldsymbol{u}) \approx\ & \delta\Pi(\varrho_{(n)}, \boldsymbol{u}_{(n)}) \\ & + \Delta(\delta\Pi(\varrho_{(n)}, \boldsymbol{u}_{(n)}, \Delta\boldsymbol{u}))\,.\end{aligned} \tag{29}$$

Albeit $\delta\Pi$ only exhibits a variation in $\boldsymbol{u}$, $\delta\Pi$ was written as a function of ϱ and $\boldsymbol{u}$ to indicate the used time-step of each quantity. The same Taylor expansion is applied to the incremental constitutive function, which, by defining $\Delta\boldsymbol{\varepsilon} = \mathrm{Grad}(\Delta\boldsymbol{u})$, can be stated as

$$\hat{\boldsymbol{\sigma}}(\varrho_{(n)}, \boldsymbol{\varepsilon}_{(n+1)}) \approx \hat{\boldsymbol{\sigma}}(\varrho_{(n)}, \boldsymbol{\varepsilon}_{(n)}) + \Delta\hat{\boldsymbol{\sigma}}(\varrho_{(n)}, \boldsymbol{\varepsilon}_{(n)}, \Delta\boldsymbol{\varepsilon})\,. \tag{30}$$

The variation of the incremental constitutive function can be found by defining the trial strain $\boldsymbol{\varepsilon}^*_{(n+1)} = \boldsymbol{\varepsilon}_{(n)} + \Delta\boldsymbol{\varepsilon}$ and applying the chain rule:

$$\begin{aligned}&\Delta\hat{\boldsymbol{\sigma}}(\varrho_{(n)}, \boldsymbol{\varepsilon}_{(n)}, \Delta\boldsymbol{\varepsilon}) \\ &= \left[\left.\frac{\mathbb{C}(\varrho_{(n)} + \Delta\varrho)}{\partial\boldsymbol{\varepsilon}^*_{(n+1)}}\right|_t : \boldsymbol{\varepsilon}^*_{(n+1)} + \mathbb{C}(\varrho_{(n)} + \Delta\varrho)\right] : \Delta\boldsymbol{\varepsilon} \\ &= \bar{\mathbb{C}}_{(n+1)} : \Delta\boldsymbol{\varepsilon}\,,\end{aligned} \tag{31}$$

where $\bar{\mathbb{C}}$ is the consistent tangent modulus. We can then further define the known principle of virtual work at time-step $t_{(n)}$:

$$\delta\Pi(\varrho_{(n)}, \boldsymbol{u}_{(n)}) = \delta U_{(n)} - \delta W_{(n)}\,, \tag{32}$$

and the increment of the virtual work:

$$\Delta(\delta\Pi(\varrho_{(n)}, \boldsymbol{u}_{(n)}, \Delta\boldsymbol{u})) = \Delta\delta U_{(n)} - \Delta\delta W_{(n)}\,, \tag{33}$$

with the virtual work of internal forces at time-step $t_{(n)}$ being defined as

$$\delta U_{(n)} = \int_{\mathcal{B}_0} \delta\boldsymbol{\varepsilon} : \boldsymbol{\sigma}_{(n)}\,\mathrm{d}V = \int_{\mathcal{B}_0} \delta\boldsymbol{\varepsilon} : \hat{\boldsymbol{\sigma}}(\varrho_{(n)}, \boldsymbol{\varepsilon}_{(n)})\,\mathrm{d}V\,, \tag{34}$$

the virtual work of the external forces at time-step $t_{(n)}$ as

$$\delta W_{(n)} = \int_{\Gamma_\sigma} \delta\boldsymbol{u} \cdot \boldsymbol{t}_{(n)}\,\mathrm{d}A\,, \tag{35}$$

and the increments of the internal virtual work and the external virtual work as

$$\Delta\delta U_{(n)} = \int_{\mathcal{B}_0} \delta\boldsymbol{\varepsilon} : \bar{\mathbb{C}}_{(n+1)} : \Delta\boldsymbol{\varepsilon}\,\mathrm{d}V \tag{36}$$

and

$$\Delta\delta W_{(n)} = \int_{\Gamma_\sigma} \delta\boldsymbol{u} \cdot \Delta\boldsymbol{t}\,\mathrm{d}A\,, \tag{37}$$

respectively, with $\Delta\boldsymbol{t} = \boldsymbol{t}_{(n+1)} - \boldsymbol{t}_{(n)}$. Summarizing all of the above, the resultant linearized weak form can be stated as

$$\begin{aligned}\int_{\mathcal{B}_0} \delta\boldsymbol{\varepsilon} : \bar{\mathbb{C}}_{(n+1)} : \Delta\boldsymbol{\varepsilon}\,\mathrm{d}V =\ & \int_{\Gamma_\sigma} \delta\boldsymbol{u} \cdot \boldsymbol{t}_{(n+1)}\,\mathrm{d}A \\ & - \int_{\mathcal{B}_0} \delta\boldsymbol{\varepsilon} : \boldsymbol{\sigma}_{(n)}\,\mathrm{d}V\,.\end{aligned} \tag{38}$$

3.4 Discretization in space

In the following, Voigt's notation $\tilde{\mathbf{a}}$ for symmetric tensors $\mathbf{a}$ is used. Presuming a standard discretization strategy of $\mathcal{B}_0$ with Lagrangian finite elements, a discretized weak form for a generic finite element e can be stated as

$$\begin{aligned}&(\delta\tilde{\boldsymbol{u}}^e)^{\mathrm{T}} \underbrace{\int_{\mathcal{B}_e} \mathbf{B}^{\mathrm{T}}\,\bar{\tilde{\mathbb{C}}}_{(n+1)}\,\mathbf{B}\,\mathrm{d}V}_{\mathbf{K}^e_{(n+1)}}\ \Delta\hat{\tilde{\boldsymbol{u}}}^e \\ &= (\delta\tilde{\boldsymbol{u}}^e)^{\mathrm{T}}\Bigg[\underbrace{\int_{\Gamma_{\sigma_e}} \mathbf{H}^{\mathrm{T}}\,\hat{\tilde{\boldsymbol{t}}}^e_{(n+1)}\,\mathrm{d}A}_{\boldsymbol{f}^{e,\mathrm{ext}}_{(n+1)}} - \underbrace{\int_{\mathcal{B}_e} \mathbf{B}^{\mathrm{T}}\,\tilde{\boldsymbol{\sigma}}_{(n)}\,\mathrm{d}V}_{\boldsymbol{f}^{e,\mathrm{int}}_{(n)}}\Bigg]\,,\end{aligned} \tag{39}$$

where $\hat{\tilde{\boldsymbol{u}}}^e$ is the element displacement vector, $\mathbf{H}$ is the element displacement field interpolation matrix and $\mathbf{B}$ is the element strain interpolation matrix. $\hat{\tilde{\boldsymbol{u}}}^e$, and $\mathbf{B}$ are chosen such that multiplying results in Voigt notated strains:

$$\tilde{\boldsymbol{\varepsilon}} = \mathbf{B}\,\hat{\tilde{\boldsymbol{u}}}^e\,. \tag{40}$$

Note, since Eq. (39) has to hold for arbitrary admissible virtual displacement fields $\delta\boldsymbol{u}$, the equivalent system of equations for an element e is written as

$$\mathbf{K}^e_{(n+1)}\,\Delta\hat{\tilde{\boldsymbol{u}}}^e = \boldsymbol{f}^{e,\mathrm{ext}}_{(n+1)} - \boldsymbol{f}^{e,\mathrm{int}}_{(n)}\,. \tag{41}$$

Subsequently, the assembled system satisfying the mechanical equilibrium equations is written as

$$\mathbf{K}_{(n+1)}\,\Delta\hat{\tilde{\boldsymbol{u}}} = \boldsymbol{f}^{\text{ext}}_{(n+1)} - \boldsymbol{f}^{\text{int}}_{(n)}\,, \tag{42}$$

which can be solved for the unknown incremental displacements $\Delta\hat{\tilde{\boldsymbol{u}}}$, provided valid boundary conditions have been incorporated into the system of equations. For more information on finite element modeling and spatial discretization, the reader is referred to [43] or [6].

3.5 Non-linear solution: the Newton-Raphson scheme

In order to solve the non-linear equation (27), the iterative Newton-Raphson method is employed. The Newton-Raphson iteration counter will be denoted by a superscript (k) in parentheses, with the first iteration starting at $k = 1$, while global time increments will be denoted by a subscript (t) in parentheses.

For the first global time-step, the global displacement vector and the bone mineral density have to be initialized:

$$\hat{\tilde{\boldsymbol{u}}}_{(0)} = \mathbf{0} \quad \text{and} \quad \varrho_{(0)} = \varrho_0\,, \tag{43}$$

where ϱ_0 is an initial bone mineral density field that can be chosen arbitrarily as long as it does not contradict any of the requirements made above. Note that the displacement field is initialized at the nodal positions while the bone mineral density is initialized at the integration points. Presuming, the solution $\hat{\tilde{\boldsymbol{u}}}_{(n)}$ is known, the updated solution vector

$$\hat{\tilde{\boldsymbol{u}}}_{(n+1)} \approx \hat{\tilde{\boldsymbol{u}}}^{(m-1)}_{(n+1)} + \Delta\hat{\tilde{\boldsymbol{u}}}^{(m)} = \hat{\tilde{\boldsymbol{u}}}_{(n)} + \sum_{i=1}^{m-1} \Delta\hat{\tilde{\boldsymbol{u}}}^{(i)} + \Delta\hat{\tilde{\boldsymbol{u}}}^{(m)} \tag{44}$$

is computed from the increments $\Delta\hat{\tilde{\boldsymbol{u}}}^{(k)}$ of a converged Newton-Raphson procedure with (m) iterations. An incremental version of the weak form (39) at $\bar{t} = t_{(n)} + \sum_{i=1}^{k-1} \Delta t^{(i)}$ can be stated as

$$(\delta\tilde{\boldsymbol{u}}^e)^{\mathrm{T}} \underbrace{\int_{\mathcal{B}_e} \mathbf{B}^{\mathrm{T}}\, \bar{\tilde{\mathbb{C}}}^{(k)}_{(n+1)}\, \mathbf{B}\, \mathrm{d}V}_{\mathbf{K}^{e(k)}_{(n+1)}}\, \Delta\hat{\tilde{\boldsymbol{u}}}^{e(k)}$$

$$= (\delta\tilde{\boldsymbol{u}}^e)^{\mathrm{T}} \Bigg[\underbrace{\int_{\Gamma_{\sigma_e}} \mathbf{H}^{\mathrm{T}}\, \hat{\tilde{\boldsymbol{t}}}^e_{(n+1)}\, \mathrm{d}A}_{\boldsymbol{f}^{e,\text{ext}}_{(n+1)}} - \underbrace{\int_{\mathcal{B}_e} \mathbf{B}^{\mathrm{T}}\, \tilde{\boldsymbol{\sigma}}^{(k)}_{(n+1)}\, \mathrm{d}V}_{\boldsymbol{f}^{e,\text{int}(k)}_{(n+1)}} \Bigg]. \tag{45}$$

In the above, the algorithmic consistent material tangent can be derived as

$$\bar{\tilde{\mathbb{C}}}^{(k)}_{(n+1)} = \left.\frac{\tilde{\mathbb{C}}(\varrho_{(n)} + \Delta\varrho^{(k)})}{\partial\tilde{\boldsymbol{\varepsilon}}^*_{(n+1)}}\right|_{\bar{t}} : \tilde{\boldsymbol{\varepsilon}}^{\text{tr},(k)}_{(n+1)} + \tilde{\mathbb{C}}(\varrho_{(n)} + \Delta\varrho^{(k)})\,, \tag{46}$$

where the iterative trial strains

$$\tilde{\boldsymbol{\varepsilon}}^{\text{tr},(k)}_{(n+1)} = \tilde{\boldsymbol{\varepsilon}}_{(n)} + \sum_{i=1}^{k-1} \Delta\tilde{\boldsymbol{\varepsilon}}^{(i)} \tag{47}$$

are defined at the integration points, and the stresses are given by

$$\tilde{\boldsymbol{\sigma}}^{(k)}_{(n+1)} = \tilde{\boldsymbol{\sigma}}_{(n)} + \sum_{i=1}^{k-1} \Delta\tilde{\boldsymbol{\sigma}}^{(i)}_{(n+1)}\,. \tag{48}$$

Note that the increment of the bone mineral density

$$\Delta\varrho^{(k)} = \Delta t\,\hat{\mathfrak{R}}(\varrho_{(n)}, \tilde{\boldsymbol{\varepsilon}}^{\text{tr},(k)}_{(n+1)}) \tag{49}$$

still only depends on the last converged bone mass density $\varrho_{(n)}$ and the trial strains $\tilde{\boldsymbol{\varepsilon}}^{\text{tr},(k)}_{(n+1)}$. Assembling the element weak form (45) results in the system of equations

$$\mathbf{K}^{(k)}_{(n+1)}\,\Delta\hat{\tilde{\boldsymbol{u}}}^{(k)} = \boldsymbol{f}^{\text{ext}}_{(n+1)} - \boldsymbol{f}^{\text{int}(k)}_{(n+1)}\,, \tag{50}$$

which is solved for the unknown increment $\Delta\hat{\tilde{\boldsymbol{u}}}^{(k)}$. The Newton-Raphson iterations are repeated until, for some time-step (m), the procedure is said to be converged, if the following condition is fulfilled:

$$\frac{||\Delta\hat{\tilde{\boldsymbol{u}}}^{(m)} - \Delta\hat{\tilde{\boldsymbol{u}}}^{(m-1)}||}{||\Delta\hat{\tilde{\boldsymbol{u}}}^{(1)}||} < \epsilon_{\text{tol}}\,, \tag{51}$$

where ϵ_{tol} is a user-defined parameter. Once convergence is achieved, the bone mineral density is updated:

$$\varrho_{(n+1)} = \varrho_{(n)} + \Delta\varrho^{(m)}\,. \tag{52}$$

Algorithm 1 Material subroutine

1: **procedure** RESPONSE($\tilde{\boldsymbol{\varepsilon}}^{(k)}_{(n+1)}, \varrho_{(n)}$)
2: $\quad \Delta\varrho^{(k)} \leftarrow \Delta t \mathfrak{R}(\varrho_{(n)}, \tilde{\boldsymbol{\varepsilon}}^{(k)}_{(n+1)})$
3: $\quad \bar{\tilde{\mathbb{C}}}^{(k)}_{(n+1)} \leftarrow \left.\frac{\tilde{\mathbb{C}}(\varrho_{(n)}+\Delta\varrho^{(k)})}{\partial\tilde{\boldsymbol{\varepsilon}}^{*}_{(n+1)}}\right|_{\tilde{\boldsymbol{\varepsilon}}^{(k)}_{(n+1)}} : \tilde{\boldsymbol{\varepsilon}}^{(k)}_{(n+1)} + \tilde{\mathbb{C}}(\varrho_{(n)} + \Delta\varrho^{(k)})$
4: $\quad$ **return** $(\bar{\tilde{\mathbb{C}}}^{(k)}_{(n+1)}, \Delta\varrho^{(k)})$

4 Strain energy density-driven bone remodeling

In Sect. 2, a thermodynamic consistent constitutive law describing bone remodeling has been proposed. The balance of mass has been defined in Eq. (3), while the mass source $\mathfrak{R}$ was left to be defined. According to the principle of thermodynamic determinism $\mathfrak{R} = \mathfrak{R}(\varrho, \boldsymbol{\varepsilon})$ has to be a function of the state variables $\{\varrho, \boldsymbol{\varepsilon}\}$. In this work, a strain energy density-driven bone remodeling approach is adopted. In [3] a strain energy density approach of the form

$$\mathfrak{R} = c\left(\Psi - \Psi^{\mathrm{ref}}\right), \tag{53}$$

has been introduced, where

$$\Psi = \varrho\psi = \varrho\left(\frac{\varrho}{\varrho_0}\right)^{n}\psi^{\mathrm{LE}} \tag{54}$$

is the density-weighted strain energy density for a linear elastic material restricted to small deformations [see Eq. (13)], Ψ^{ref} is a physiological target value that should be adopted by the density-weighted strain energy density, and c is an additional parameter with the unit time divided by area, which governs the speed of the bone remodeling process. In [19] a extension of this approach has been suggested

$$\begin{aligned}\mathfrak{R} &= c\left(\left(\frac{\varrho}{\varrho_0}\right)^{-m}\Psi - \Psi^{\mathrm{ref}}\right)\\ &= c\left(\varrho\left(\frac{\varrho}{\varrho_0}\right)^{n-m}\psi^{\mathrm{LE}} - \Psi^{\mathrm{ref}}\right),\end{aligned} \tag{55}$$

by the introduction of an additional factor $(\varrho/\varrho_0)^{-m}$. By setting $m = 0$ the approach of [3] is recovered, while it has been shown that by choosing $m > n$, uniqueness and stability of the solution is guaranteed [19]. The necessity of the stability criterion $m > n$ for strain energy density-driven bone remodeling, as introduced in Eq. (55), can be demonstrated by the following example: For an arbitrary point in the continuum we choose $\varrho_0 = 1$ g/cm³, $n = 2$, $\Psi^{\mathrm{LE}} = \varrho\psi^{\mathrm{LE}} = 0.1$ g/cm³, $\Psi^{\mathrm{ref}} = 0.05$ g/cm³, and $\Delta t \cdot c = 1$ s²/m. Since Ψ^{ref} is to be adapted by Ψ^{LE}, it is clear that the actual bone mass density ϱ must increase. In Fig. 1, the change of density $\Delta\varrho$ is plotted for $m = 0$ and $m = 3$ over all possible actual mass densities $\varrho \in [0.1, 2]$. For $m = 0$, it becomes visible that, contrary to the physiologically desired behavior, bone mass density decreases for small actual values of bone mass density. As the actual density gets larger, the change in bone mass density increases quadratically. In contrast, for $m = 3$, the largest change in bone mass density occurs with small actual values of bone mass density and decreases as the actual value increases, which can be seen as a saturation effect. While the former example promotes checkerboard patterns due to the unphysiological behavior, the latter suppresses these patterns successfully.

5 Material subroutine

During the integration of the local stiffness matrix

$$\mathbf{K}^{e}_{(n+1)} = \int_{\mathcal{B}_e} \mathbf{B}^{\mathrm{T}}\,\bar{\tilde{\mathbb{C}}}_{(n+1)}\,\mathbf{B}\,\mathrm{d}V\,, \tag{56}$$

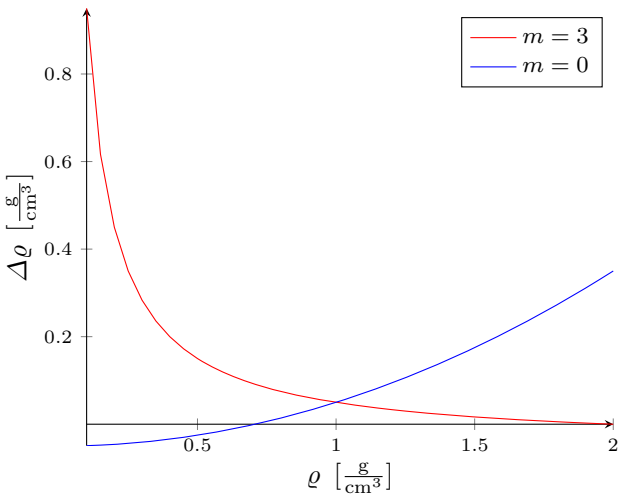

Fig. 1 Change of bone mass density depending on the current bone mass density

the algorithmic consistent tangent modulus (46) is evaluated at the supporting points of the numerical integration scheme. Consequently, state variables $\{\varrho, \varepsilon\}$ are discretized and stored at the integration points. Thus, the nature of bone remodeling only manifests itself in the material subroutine of the finite element framework.

Consider a global time-step $[t_{(n)}, t_{(n+1)}]$ and a Newton-Raphson iteration (k). At each integration point $\boldsymbol{X}_I$, the material subroutine is executed with the trial strains

$$\tilde{\boldsymbol{\varepsilon}}^{(k)}_{(n+1)} = \hat{\boldsymbol{\varepsilon}} \left(\boldsymbol{X}_I, \tilde{\boldsymbol{\varepsilon}}(\boldsymbol{X}_I, t_{(n)}), \Delta\tilde{\boldsymbol{\varepsilon}} \left(\boldsymbol{X}_I, t_{(n)} + \sum_{i=1}^{k-1} \Delta t^{(i)} \right) \right) \tag{57}$$

and the last converged state of the bone mineral density $\varrho_{(n)} = \varrho(\boldsymbol{X}_I, t_{(n)})$ as input arguments. By recalling that within the Newton-Raphson iteration of a time-step $[t_{(n)}, t_{(n+1)}]$, **only** the trial strains are allowed to be altered (cf. [12]), it gets clear that for obtaining the iterative change in bone mineral density

$$\Delta\varrho^{(k)} = \Delta t \mathfrak{R}(\varrho_{(n)}, \tilde{\boldsymbol{\varepsilon}}^{(k)}_{(n+1)}) \tag{58}$$

only an evaluation of the function $\mathfrak{R}$ is necessary since the quantities $\varrho_{(n)}$ and $\tilde{\boldsymbol{\varepsilon}}^{(k)}_{(n+1)}$ are known, and no internal Newton-scheme is necessary. The material subroutine is briefly summarized in Algorithm 1.

5.1 Principle of static-equivialent forces and related biomechanical-equilibrated bone-mineral density distribution

At this point, it shall be noted that bone remodeling is a *long-term process* that takes place over a period of years. This justifies the omission of dynamic forces if the quantity of interest is a biomechanical-equilibrated bone-mineral density distribution [11,20,28].

Now consider a quasi-static example for a linearized-weak form of type (38) for a non-linear but time-independent material: if the surface loads are held constant between two time-steps $t_{(n)}$ and $t_{(n+1)}$, no Newton-Raphson iteration would take place since the external forces $\boldsymbol{f}^{\text{ext}}_{(n+1)}$ are already in balance with the internal force $\boldsymbol{f}^{\text{int}}_{(n)}$.

Contrary, in bone remodeling as described here, two (pseudo)-time constants were introduced: (1) Δt for the implicit Euler time integration and (2) c as a constant describing the process speed in equation (53). That results in a possibly out-of-balance right-hand side, although forces are held constant between two time-steps. By that, it is possible to define a biomechanical-equilibrated bone-mineral density distribution: assume $\boldsymbol{t} = \boldsymbol{t}(\boldsymbol{X})$ and $\varrho = \varrho(\boldsymbol{X})$ are given surface loads and a given bone mineral density distribution,

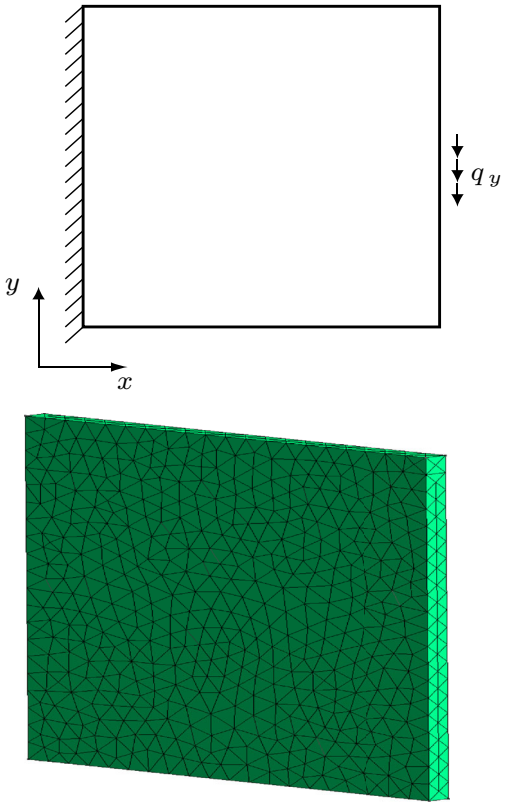

Fig. 2 Thin plate model: schematic representation (top) and sample discretization (bottom)

respectively. $\varrho(\boldsymbol{X})$ is called biomechanical-equilibrated with respect to $\boldsymbol{t}$, if $\boldsymbol{\sigma}_{(n+1)} = \boldsymbol{\sigma}_{(n)}$ for $\boldsymbol{t}_{(n+1)} = \boldsymbol{t}_{(n)} = \boldsymbol{t}$.

It is noted here that, albeit being unconditionally stable for many problems, the time discretization constant Δt in the backward Euler method cannot be chosen arbitrarily large in order for the Newton-Raphson procedure to converge.

What remains is a meaningful definition of $\boldsymbol{t}$: in [28], surface loads were computed by solving the inverse optimization problem

$$\min_{\boldsymbol{t}} \frac{1}{2} \sum_{I=1}^{\text{n}_{\text{elems}}} (\varrho(\boldsymbol{X}_I, \boldsymbol{\varepsilon}) - \varrho^{\text{ref}}(\boldsymbol{X}_I))^2 , \tag{59}$$

where $\varrho^{\text{ref}}(\boldsymbol{X}_I)$ has been obtained by projecting 3D-CT data from a human femur to an associated finite element mesh.

6 Numerical examples

In this section, numerical examples demonstrate the correct implementation of the bone remodeling algorithm. The entire project was implemented independently in the julia language [4]. Neither commercial nor open-source finite element software has been used. MUMPS [1] has been used as a solver

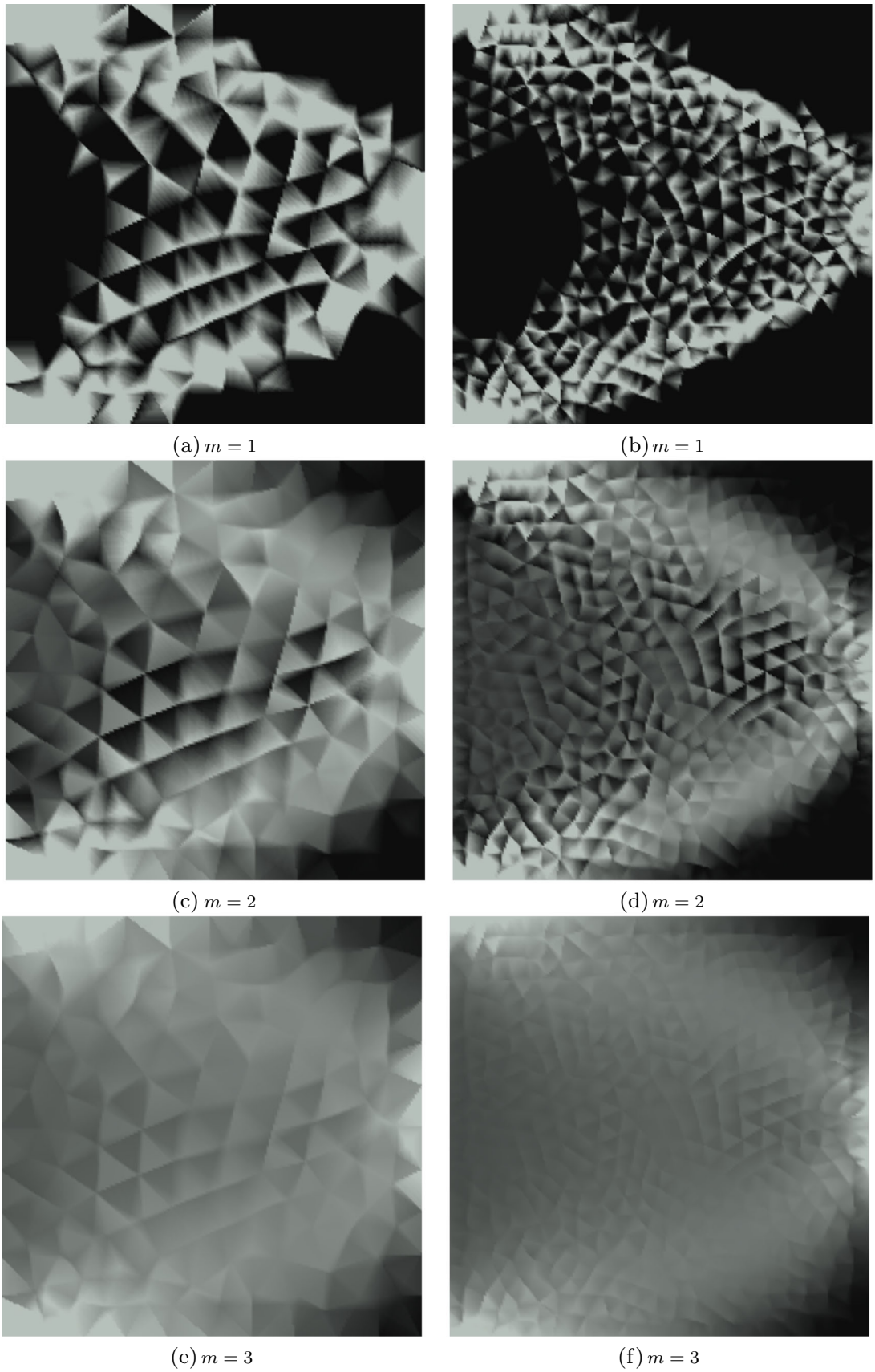

(a) $m = 1$ (b) $m = 1$

(c) $m = 2$ (d) $m = 2$

(e) $m = 3$ (f) $m = 3$

Fig. 3 Bone remodeling followed by X-ray simulation of thin plate model meshed by linear tetrahedral elements. The left-hand side pictures are derived from the coarse mesh; the right-hand side pictures from the finer mesh

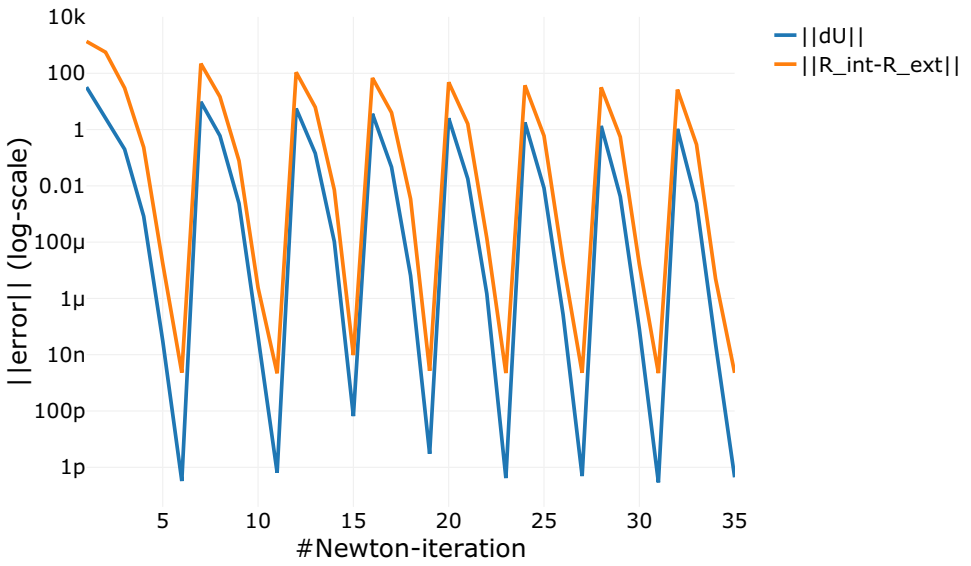

Fig. 4 Convergence history of bone remodeling material model depicted by the number of Newton iteration for 8 external load steps. Depicted is the l^2-norm of the increment of the displacement vector and the l^2-norm of the residuum

for the linear system of equations. The first example is a thin plate where the variation of the parameter m shall be investigated. The second example is the human femur, where the influence of the reference strain energy Ψ^{ref} is studied.

For both examples following assumptions are made: to define the bone material, the parameters introduced in (17) are used. The shear modulus is set to $\nu = 0.3$, and a combined parameter $\Delta t \cdot c = 50\ \text{s}^2/\text{m}$ is used for controlling the speed of the adaption process. The force is constant and the maximum number of global time-steps is $(n_{\max}) = 120$. The algorithm is said to be converged if, for some timestep $1 < k \leq n$: $|\varrho_{(k)}(\boldsymbol{X}_I) - \varrho_{(k-1)}(\boldsymbol{X}_I)| < \epsilon_{\text{tol}}$ for all integration points $\boldsymbol{X}_I$. All results are transferred to X-ray images according to [5] since the internal bone mineral distribution is easier to infer from a reduced representation. As a result no smoothing of the results from post-processing has taken place. Note that no color scale is given as this is an arbitrary result of the calibration of the X-ray simulation attenuation law. For a rigorous calibration, one would need several X-ray images of different specimens produced with a standardized X-ray device. Since this was not done, the results are only a demonstration of the performance of the presented method.

All simulation start with a homogenous bone mineral distribution with $\varrho_{(0)}(\boldsymbol{X}_I) = 1\ \text{g/cm}^3$ for all integration points $\boldsymbol{X}_I$. It shall be mentioned here that the simulation converges to the same results, even if the bone mineral density is modeled as an appropriate smooth Gaussian random field. For this case, the number of external load steps necessary increases significantly. As a remark, it can be stated that in the convergent case, the increment of the bone mineral density field $||\Delta\boldsymbol{\varrho}|| = ||\boldsymbol{\varrho}_{(n)} - \boldsymbol{\varrho}_{(n-1)}||$ decreases monotonically over the load steps for a constant load vector $\boldsymbol{t}_{(n+1)} = \boldsymbol{t}_{(n)} = \boldsymbol{t}$.

6.1 Model 1: thin plate

As a first example, a thin three-dimensional plate with dimensions of $20\,\text{cm} \times 20\,\text{cm} \times 1\,\text{cm}$ is clamped on its left-hand side, and a shear force $q_y(y) = 1\ \text{kN/mm}$ at $9\,\text{cm} \leq y \leq 11\,\text{cm}$ is applied at the right-hand side as displayed in Fig. 2. The reference strain energy density is set to $\Psi^{\text{ref}} = 10^{-3}\ \text{N/mm}^2$. The exponent m is varied in order to study the influence of this parameter. The results of X-ray simulations of the thin plate following the bone remodeling process are shown in Fig. 3 for linear shape functions and in Fig. 5 for quadratic shape functions.

Finite elements with linear shape functions. The thin plate model is discretized by linear four-node tetrahedral elements, resulting in a mesh with 709 elements and 816 degrees of freedom by choosing a coarse discretization scheme or, for a finer discretization scheme, in a mesh with 3081 elements and 3267 degrees of freedom.

For the exponent $m = 1$, it can be seen that strong *checkerboard* patterns occur for both discretizations, the coarse one shown in Fig. 3a and the finer one displayed in Fig. 3b. Therefore, convergence of the global algorithm is not achieved, while quadratic convergence of the Newton-Raphson method is preserved in almost every load step, as shown in Fig. 4. It should be noted that the quadratic convergence rate is missed when too large load steps are applied, which is probably the case at the beginning of each simulation or when the residual becomes too small due to the numerical tangent modulus used. As the exponent m increases, the bone mineral density distribution gets smoother, as seen by comparing Fig. 3c, e or Fig. 3d, f, respectively. Still, unphysical checkerboard-like patterns are not entirely suppressed. As all the results exhibit unphysical patterns, it can be concluded that linear finite elements are unsuitable to perform bone remodeling

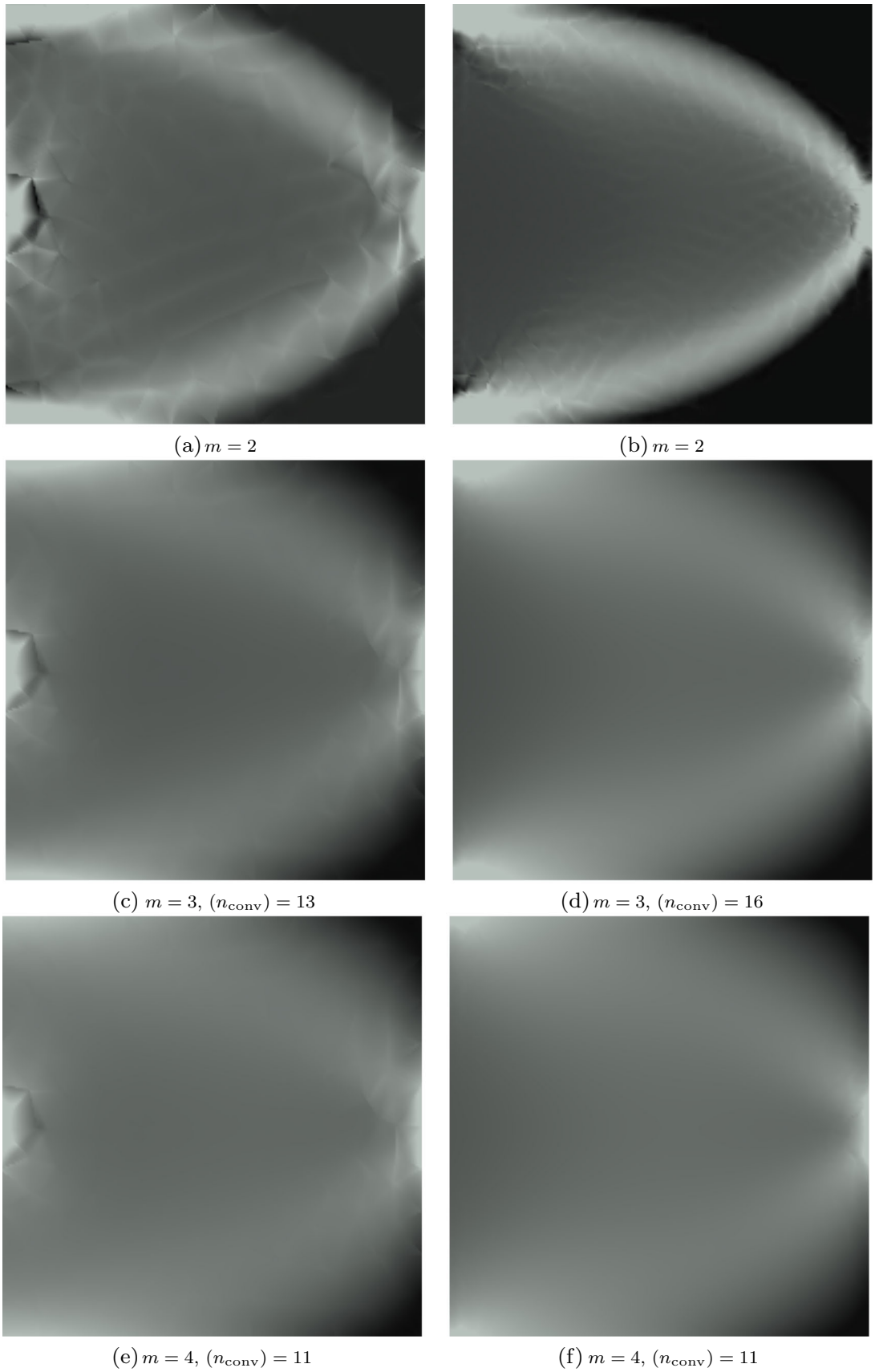

(a) $m = 2$ (b) $m = 2$

(c) $m = 3$, $(n_{\mathrm{conv}}) = 13$ (d) $m = 3$, $(n_{\mathrm{conv}}) = 16$

(e) $m = 4$, $(n_{\mathrm{conv}}) = 11$ (f) $m = 4$, $(n_{\mathrm{conv}}) = 11$

Fig. 5 Bone remodeling followed by X-ray simulation of thin plate model meshed by quadratic tetrahedral elements. The left-hand side pictures are derived from the coarse mesh; the right-hand side pictures from the finer mesh

simulations, without further treatment of these effects, with the methods described here.

Quadratic finite elements The thin plate model is discretized by quadratic ten-node tetrahedral elements, resulting in a mesh with 709 elements and 4566 degrees of freedom by choosing a coarse discretization scheme or, if a finer discretization scheme is applied, in a mesh with 3081 elements and 19,032 degrees of freedom. For simulations with $m = 1$ (not depicted), convergence of the global algorithm was not achieved, and unphysical patterns could be seen. For $m = 2$, the same unphysical patterns occur but are less pronounced, as seen in Fig. 5a or b. The exponent being $m = 3$ is the first case where no unphysical patterns are visible, and the global algorithm converges in 13 steps for the coarse mesh and 16 steps for the finer mesh. In Fig. 5c, disturbances can be seen near the support and force application, but these phenomena disappear if the mesh is refined, as seen in Fig. 5b. It can be observed that while m increases, global convergence is enhanced in general. The Newton-Raphson scheme preserved quadratic convergence as discussed for linear elements in the previous example.

6.2 Example 2: human femur

A human femur serves as a second example. Boundary and loading conditions were straightforwardly adopted from [27], where loading conditions for the quasi-static case were calculated by solving the inverse problem stated in (59). A total net force of 382 N was applied to the femur. The distribution of the applied forces can be seen in Fig. 6. This static load-equivalent leads to a biomechanical-equilibrated bone-mineral density distribution (cf. Sect. 5.1), which approximately corresponds to the psychological distribution. For more information on boundary and loading conditions for the quasi-static case and the solution of the inverse problem, the reader is referred to [27,28]. Since linear finite elements did not perform sufficiently in the last example, the model is meshed solely by ten-node quadratic tetrahedral elements, resulting in 21,451 elements and 102,048 degrees of freedom. The exponent m is set to $m = 4$ since this setting resulted in the fastest convergence rate in the last example. At the same time, the reference strain energy density is altered to study its influence. The results are transferred to X-ray images and depicted in Fig. 7. In Fig. 7a, it can be seen that $\Psi^{\text{ref}} = 0.00001\ \text{N/mm}^2$ is too small as a reference strain energy density and leads to a bone mineral density distribution that is nearly uniform and doesn't develop visible zones of compact and cancellous bone. Increasing Ψ^{ref} leads to bone mineral density distribution which can be considered more realistic, as seen in Fig. 7b or, with even more prominent developed zones with compact and cancellous bone, in Fig. 7c. In Fig. 7d, it can be concluded that $\Psi^{\text{ref}} = 0.001\ \text{N/mm}^2$ is too large as a reference strain energy with regard to the force applied since, especially in the region of the femoral head, the bone mineral density seems to be underdeveloped. By that, it can be concluded that $0.0005 \leq \Psi^{\text{ref}} < 0.001$ can be considered an optimal reference strain energy with respect to the given model, boundary, and loading conditions. It should be noted that these are only preliminary evaluations. For a proper evaluation, a comparison with medical studies would be necessary, which was not done here. Finally, it can be stated that for this example, the Newton-Raphson algorithm preserved quadratic convergence as described for the previous models, and the global algorithm has converged in less than 15 time-steps. The computation time can be specified with less than 10 min on a desktop PC with Intel Core i7 8700k with 32 GB DDR 4 RAM.

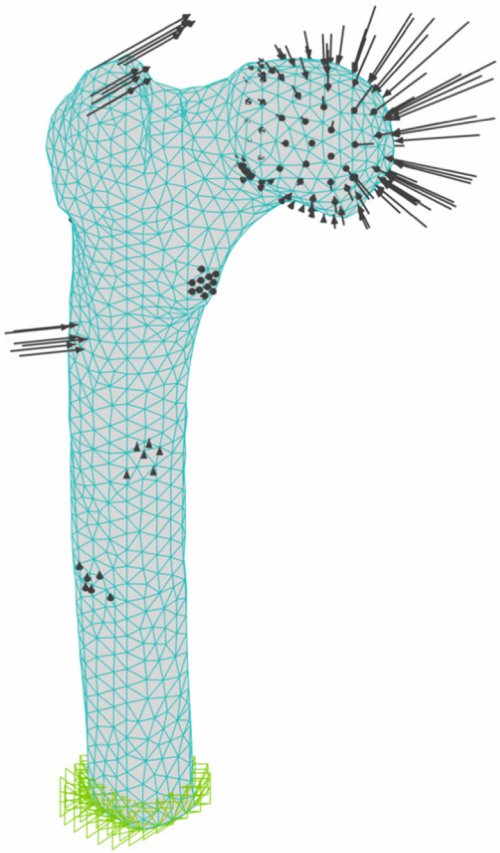

Fig. 6 Finite element model of human femur with boundary and loading conditions

7 Conclusion

In this work, a fully implicit finite element material model for bone remodeling was provided. The theory of open systems was used to derive a thermodynamically consistent description of bone remodeling in analogy to [24]. In delimitation thereof, incorporating the constitutive relations into the finite

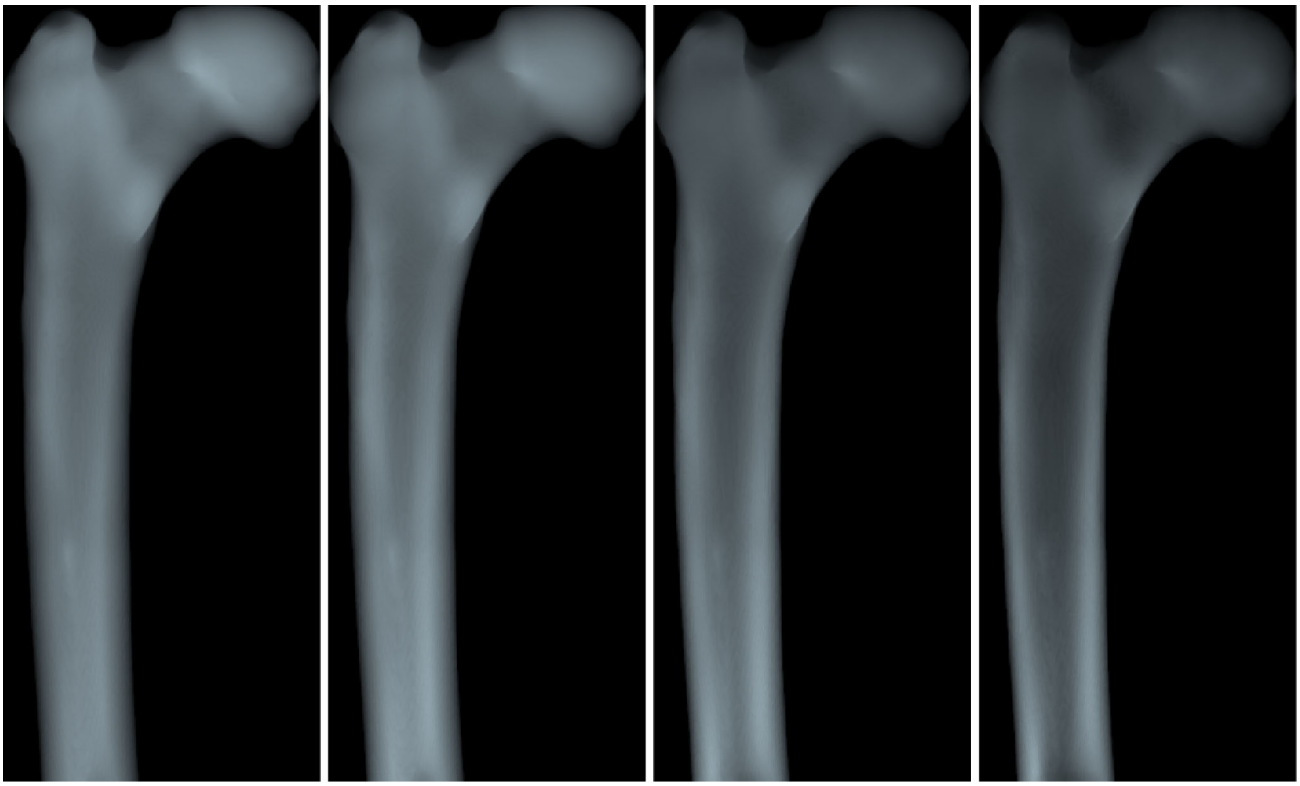

Fig. 7 Bone remodeling followed by X-ray simulation of a human femur with different reference strain energy densities Ψ^{ref}

element framework was done analogously to material modeling, as described in [12]. This ultimately results in a novel description of bone remodeling as a fully implicit and consistent finite element material model. Due to the fully implicit description, it is possible to implement bone remodeling very efficiently into any standard finite element framework with shape functions of quadratic or higher order. The additional computational costs caused by the quadratic shape functions can be easily outweighed by the ability of quadratic finite elements to model rounded objects by many fewer elements. The functionality of the described method was demonstrated with two numerical examples.

The unsuitability of linear shape functions, with the methods used in this work, can be explained by the resulting element-wise constant strains. This results in element-wise constant strain energy densities, which are then adopted by the bone mass density. It is noted that these and other unphysical patterns, as depicted in Figs. 3e, f and 5c, d, would not be readily visible from a standard finite element post-processing. From that, it can be concluded that the results shown in Fig. 7 are smooth on the integration point level without any need for further numerical treatment.

Funding Open Access funding enabled and organized by Projekt DEAL.

References

1. Amestoy PR, Duff IS, L'Excellent JY, Koster J (2000) Mumps: a general purpose distributed memory sparse solver. In: International workshop on applied parallel computing. Springer, pp 121–130
2. Beaupré G, Orr T, Carter D (1990) An approach for time-dependent bone modeling and remodeling—application: a preliminary remodeling simulation. J Orthop Res 8(5):662–670
3. Beaupré G, Orr T, Carter D (1990) An approach for time-dependent bone modeling and remodeling—theoretical development. J Orthop Res 8(5):651–661
4. Bezanson J, Edelman A, Karpinski S, Shah VB (2017) Julia: a fresh approach to numerical computing. SIAM Rev 59(1):65–98
5. Bittens M (2021) Technical report: virtual X-ray imaging for higher-order finite element results. arXiv:2105.02651

6. Braess D (2013) Finite Elemente: Theorie, schnelle Löser und Anwendungen in der Elastizitätstheorie. Springer, Berlin
7. Calvo-Gallego JL, Pivonka P, García-Aznar JM, Martínez-Reina J (2021) A novel algorithm to resolve lack of convergence and checkerboard instability in bone adaptation simulations using nonlocal averaging. Int J Numer Methods Biomed Eng 37(2):e3419
8. Carter D, Fyhrie D, Whalen R (1987) Trabecular bone density and loading history: regulation of connective tissue biology by mechanical energy. J Biomech 20(8):785–794
9. Carter D, Orr T, Fyhrie D (1989) Relationships between loading history and femoral cancellous bone architecture. J Biomech 22(3):231–244
10. Carter DR, Hayes WC (1977) The compressive behavior of bone as a two-phase porous structure. J Bone Joint Surg Am Vol 59(7):954–962
11. Cowin S, Hegedus D (1976) Bone remodeling I: theory of adaptive elasticity. J Elast 6(3):313–326
12. de Souza Neto EA, Peric D, Owen DR (2011) Computational methods for plasticity: theory and applications. Wiley, Hoboken
13. Doblaré M, Garcıa J (2002) Anisotropic bone remodelling model based on a continuum damage-repair theory. J Biomech 35(1):1–17
14. Epstein M, Maugin GA (2000) Thermomechanics of volumetric growth in uniform bodies. Int J Plast 16(7–8):951–978
15. Fernández J, García-Aznar J, Martínez R (2012) Numerical analysis of a diffusive strain-adaptive bone remodelling theory. Int J Solids Struct 49(15–16):2085–2093
16. Frost H (1960) The Utah paradigm of skeletal physiology. ISMNI
17. Garcia-Aznar JM, Rüberg T, Doblare M (2005) A bone remodelling model coupling microdamage growth and repair by 3D BMU-activity. Biomech Model Mechanobiol 4(2–3):147–167
18. Gibson I, Ashby MF (1982) The mechanics of three-dimensional cellular materials. Proc R Soc Lond A Math Phys Sci 382(1782):43–59
19. Harrigan T, Hamilton J (1992) Optimality conditions for finite element simulation of adaptive bone remodeling. Int J Solids Struct 29(23):2897–2906
20. Huiskes R, Weinans H, Grootenboer H, Dalstra M, Fudala B, Slooff T (1987) Adaptive bone-remodeling theory applied to prosthetic-design analysis. J Biomech 20:1135–1150
21. Idhammad A, Abdali A, Alaa N (2013) Computational simulation of the bone remodeling using the finite element method: an elastic-damage theory for small displacements. Theor Biol Med Model 10(1):32
22. Jacobs C, Levenston M, Beaupré G, Simo J, Carter D (1995) Numerical instabilities in bone remodeling simulations: the advantages of a node-based finite element approach. J Biomech 28(4):449–459
23. Kuhl E (2004) Theory and numerics of open system continuum thermodynamics: spatial and material setting. Universität Kaiserslautern, Kaiserslautern
24. Kuhl E, Menzel A, Steinmann P (2003) Computational modeling of growth. Comput Mech 32(1–2):71–88
25. Kuhl E, Steinmann P (2003) Mass- and volume-specific views on thermodynamics for open systems. Proc R Soc Lond Ser A Math Phys Eng Sci 459(2038):2547–2568
26. Liao Z, Yoda N, Chen J, Zheng K, Sasaki K, Swain MV, Li Q (2017) Simulation of multi-stage nonlinear bone remodeling induced by fixed partial dentures of different configurations: a comparative clinical and numerical study. Biomech Model Mechanobiol 16(2):411–423
27. Lutz A (2011) Ein integrales Modellierungskonzept zur numerischen Simulation der Osseointegration und Langzeitstabilität von Endoprothesen. IBNM
28. Lutz A, Nackenhorst U (2007) Computation of static-equivalent load sets for bone remodeling simulation. In: PAMM: proceedings in applied mathematics and mechanics, vol 7(1). Wiley Online Library, pp 4020007–4020008
29. Malvern LE (1965) Introduction to the mechanics of a continuous medium. Addison-Wesley Publishing Company, Boston
30. Morgan EF, Bayraktar HH, Keaveny TM (2003) Trabecular bone modulus—density relationships depend on anatomic site. J Biomech 36(7):897–904
31. Mukherjee K, Gupta S (2017) Combined bone ingrowth and remodeling around uncemented acetabular component: a multi-scale mechanobiology-based finite element analysis. J Biomech Eng 139(9)
32. Nackenhorst U, Krstin N, Lammering R (2000) A constitutive law for anisotropic stress adaptive bone remodeling. ZAMM-J Appl Math Mech/Zeitschrift für Angewandte Mathematik und Mechanik 80(S2):399–400
33. Ottosen NS, Ristinmaa M (2005) The mechanics of constitutive modeling. Elsevier, Amsterdam
34. Pauwels F (1965) Funktionelle Anpassung des Knochens durch Längenwachstum. In: Gesammelte Abhandlungen zur funktionellen Anatomie des Bewegungsapparates. Springer, pp 400–423
35. Peyroteo M, Belinha J, Dinis L, Jorge RN (2020) Bone remodeling: an improved spatiotemporal mathematical model. Arch Appl Mech 90(3):635–649
36. Schrödinger E (1944) What is life? The physical aspect of the living cell and mind. Cambridge University Press, Cambridge
37. Sotto-Maior BS, Mercuri EGF, Senna PM, Assis NMSP, Francischone CE, Del Bel Cury AA (2016) Evaluation of bone remodeling around single dental implants of different lengths: a mechanobiological numerical simulation and validation using clinical data. Comput Methods Biomech Biomed Eng 19(7):699–706
38. Taber L (1995) Biomechanics of growth, remodeling, and morphogenesis. App Mech Rev 48(8):487–545
39. Truesdell C, Flügge S, Nemat-Nasser S, Olmstead W (1975) Mechanics of solids II. J Appl Mech 42:247
40. Weinans H, Huiskes R, Grootenboer H (1992) The behavior of adaptive bone-remodeling simulation models. J Biomech 25(12):1425–1441
41. Wolff J (1892) Das Gesetz der Transformation der Knochen. Hirschwald, Berlin, pp 1–152
42. Wriggers P (2008) Nonlinear finite element methods. Springer, Berlin
43. Zienkiewicz OC, Taylor RL, Nithiarasu P, Zhu J (1977) The finite element method, vol 3. McGraw-hill, New York
44. Zienkiewicz OC, Zhu J (1992) The superconvergent patch recovery (SPR) and adaptive finite element refinement. Comput Methods Appl Mech Eng 101(1–3):207–224